Predicting 1-year in-stent restenosis in superficial femoral arteries through multiscale computational modelling

Accepted manuscript at https://doi.org/10.1098/rsif.2022.0876

Predicting 1-year in-stent restenosis in superficial femoral arteries through multiscale computational modeling

Anna Corti[1], Francesco Migliavacca[1], Scott A. Berceli[2,3], Claudio Chiastra[4,*]

1. Laboratory of Biological Structure Mechanics (LaBS), Department of Chemistry, Materials and Chemical Engineering "Giulio Natta", Politecnico di Milano, Milan, Italy
2. Department of Surgery, University of Florida, Gainesville, FL, USA
3. Malcom Randall VAMC, Gainesville, FL, USA
4. PoliTo[BIO]Med Lab, Department of Mechanical and Aerospace Engineering, Politecnico di Torino, Turin, Italy

***Address for correspondence:**

Claudio Chiastra, PhD

PoliTo[BIO]Med Lab, Department of Mechanical and Aerospace Engineering

Politecnico di Torino, Corso Duca degli Abruzzi 24, 10129 Turin, Italy

claudio.chiastra@polito.it

Accepted manuscript at https://doi.org/10.1098/rsif.2022.0876

Abstract

In-stent restenosis (ISR) in superficial femoral arteries (SFAs) is a complex, multifactorial and multiscale vascular adaptation process whose thorough understanding is still lacking. Multiscale computational agent-based modeling has recently emerged as a promising approach to decipher mechanobiological mechanisms driving the arterial response to the endovascular intervention. However, the long-term arterial response has never been investigated with this approach, although being of fundamental relevance. In this context, this study investigates the 1-year post-operative arterial wall remodeling in three patient-specific stented SFA lesions through a fully-coupled multiscale agent-based modeling framework. The framework integrates the effects of local hemodynamics and monocyte gene expression data on cellular dynamics through a bi-directional coupling of computational fluid dynamics simulations with an agent-based model of cellular activities. The framework was calibrated on the follow-up data at 1-month and 6-months of one stented SFA lesion and then applied to the other two lesions. The calibrated framework successfully captured (i) the high lumen area reduction occurring within the first post-operative month and (ii) the stabilization of the median lumen area from 1-month to 1-year follow-ups in all the stented lesions, demonstrating the potentialities of the proposed approach for investigating patient-specific short- and long-term responses to endovascular interventions.

Keywords

Lower-limb peripheral arteries, In-stent restenosis, Computational modeling, Agent-based modeling, Computational fluid dynamics, Mechanobiology

1. Introduction

Lower-limb peripheral artery disease (PAD) is a chronic occlusive pathology that affects more than 230 million people worldwide [1]. Lower-limb PAD is associated with the insurgence of atherosclerosis, with the superficial femoral artery (SFA) being the most atheroprone vessel [2]. Among the endovascular treatments, percutaneous transluminal angioplasty (PTA) with self-expanding stent implantation is one of the most widespread approaches for atherosclerotic SFAs [3]. However, the occurrence of in-stent restenosis (ISR), which ranges from 15% to 32% and peaks between 9 and 15 months post-intervention, limits the long-term patency of stented SFAs [4]. ISR consists in the degenerated inflammatory-driven healing response of the vessel to the intervention-induced trauma, which ultimately leads to lumen re-narrowing as consequence of sustained exacerbated cellular activities [5]. Different systemic, biological and biomechanical factors concur to the complex and multiscale network of events. Besides the arterial wall injury provoked by the endovascular procedure, representing the main triggering event of the early inflammatory response, the stent-induced disturbed hemodynamics has been identified to contribute to ISR initiation and progression [5].

Recently, multiscale computational agent-based modeling frameworks, coupling continuous- and agent-based approaches, emerged as a promising tool for a systems biology description of the multiscale mechanobiological interplay of events characterizing the arterial response to stent implantation [6]. This approach generally consists in integration of (i) the continuum description of the biomechanics (e.g., hemodynamics or structural mechanics) at the tissue level through numerical methods solving partial differential equations (as finite volume or finite element), with (ii) the discrete description of the cell behavior in response to the biomechanical cues at the cellular scale through an agent-based model

(ABM). To date, several multiscale agent-based modeling frameworks have been proposed for the study of ISR [6]. However, these frameworks (i) are not patient-specific, (ii) do not include gene expression data and (iii) do not simulate long-term arterial wall remodeling. Recently, Corti et al. [7] have developed a patient-specific multiscale agent-based modeling framework of ISR in SFAs, integrating the effects of local hemodynamics and monocyte gene expression (accounting for systemic inflammation) on cellular dynamics and subsequent post-intervention arterial wall remodeling. The framework consisted of a unidirectional coupling between a computational fluid dynamics (CFD) simulation (hemodynamics module) and ABM of cellular dynamics (tissue remodeling module). As pilot study, the authors performed a short-term analysis, in which the framework was used to simulate the arterial wall remodeling after stent deployment in a human SFA until 1-month follow-up. The short-term (1-month) response to the intervention is certainly of great importance in the time course of ISR in SFAs, being characterized by (i) an intense inflammation, whose markers have been identified as potential predictor of the long-term outcome (e.g., [8–11]), and (ii) the greatest and fastest lumen area change [12]. However, also the long-term response is thought to be of fundamental relevance, as ISR peak in SFAs mainly occurs between 9 and 15 months post-intervention [4,13]. In addition, a three-phase arterial wall remodeling was observed in stented SFAs along 1-year follow-up [12]. Specifically, (i) the fastest lumen area reduction was observed at 1-month follow-up, followed by (ii) a smaller lumen area change between 1-month and 6-month follow-ups, and (iii) a frequent focal lumen re-narrowing between 6-month and 1-year follow-ups [12].

Given the clinical relevance of the long-term arterial response to stenting intervention, the present work aims to investigate the arterial remodeling processes for longer post-intervention periods (i.e., up to 1-year follow-up), thus expanding the short-term analysis previously performed by Corti et al. [7].

Three stented SFA lesions of one patient were included in the study. First, the framework was adapted to account for the bi-directional interaction between the hemodynamics and tissue remodeling modules. Second, a calibration of the ABM parameters was performed by considering the follow-up data at 1-month and 6-months of one of the three patient stented SFA lesions. Third, the calibrated framework was used to simulate the 1-year arterial wall response in the three lesions of the same patient. Last, the model capability to predict the long-term post-intervention arterial wall remodeling was evaluated by comparing the simulated outputs with the patient follow-up data.

2. Methods

2.1 Patient-specific data and superficial femoral artery models

2.1.1 Clinical dataset

The same clinical dataset presented in [7] was adopted also for this work. Briefly, 14 patients suffering from PAD who underwent PTA and the placement of single or multiple EverFlex stents (EV3, Medtronic, Dublin, Ireland) in the SFA were recruited between 2007 and 2012 at the Malcom Randall VAMC (Gainesville, FL, USA). All patients consented to monocyte gene expression measurements from blood samples collected at 1 hour pre-intervention, and 2 hours, 1, 7, and 28 days post-intervention, and to the acquisition of computer tomography (CT) and Doppler ultrasound images at 1 week (baseline condition), 1 month, 6 months and 1 year post-intervention.

The framework was applied to three stented SFA lesions of a single patient. This patient was a 57-year-old male treated with (i) one stent of 40 mm in the proximal left SFA (lesion L-A), (ii) two

overlapping stents of 150 mm each (with overlapping of ~45 mm) in the distal left SFA (lesion L-B) and (iii) two overlapping stents of 120 mm and 150 mm (with overlapping of ~40 mm) in the right SFA (lesion R). Figure 1 shows the SFA models, reconstructed as described in Section 2.1.3. The study was approved by the Institutional Review Board at the University of Florida (Gainesville, FL, USA) and conformed to the Helsinki Declaration on human research of 1975, as revised in 2000.

2.1.2 Monocyte gene expression analysis

As detailed in [7], from the blood samples of the 14 patients collected at the available time points, the expression level of 34,834 monocyte genes was measured to identify clusters of genes associated with the 1-year clinical success/failure of the endovascular procedure. The clinical failure, evaluated through angiography or Doppler ultrasound, was defined as high-grade stenosis (increase in peak systolic velocity higher than 3.5-fold) or occlusion of the treated lesion, an interval decrease in ankle-brachial index higher than 15% with return of clinical symptoms, or the need for a secondary intervention [11]. Briefly, first, 1,263 time-dependent genes were identified through ANOVA test ($p<0.05$); second, the 1,263 time-dependent genes were divided into 34 clusters through a custom clustering algorithm [14]; third, the 34 clusters were filtered through a selection process identifying the clusters that were differentially expressed between outcome groups (success/failure). Three clusters containing 22 genes fulfilled the selection criteria, thus being most likely associated with the procedure outcome. Consequently, the patient average gene expression profiles of the three detected clusters were used within the framework of ISR, as representative of the patient-specific level of systemic inflammation. Figure 2 shows, for the three detected clusters, the patient average expression profile of the genes belonging to the cluster (black curve), compared to the success (green) and failure (red) curves, representing the

average gene expression profiles (of all the genes) of the patients that are part of the success and failure groups, respectively. The patient considered in the present study was part of the success group.

2.1.3 3D geometrical artery models

The lumen geometry of the two stented SFAs was reconstructed at baseline and at 1-month, 6-month and 1-year follow-ups from CT images using an in-house developed 3D reconstruction method [15]. Briefly, an active contour method, based on a level set algorithm was applied to segment the CT images. Calibrated thresholds were used to correct the segmentations and remove calcifications, metallic artifacts and thrombi. Due to the limited resolution of CT images, which does not allow for stent strut visualization and 3D reconstruction, the morphing procedure described in [16] was adopted to virtually implant the EverFlex stents into the baseline SFA models using the mesh manipulation tool HyperMorph of HyperMesh (Altair Engineering, Troy, MI, USA). Specifically, while for the lesion L-A, the model of the single 40-mm stent was virtually implanted as conducted in [7], for lesions L-B and R, first the distal stent (150-mm) and then the proximal ones (150- and 120-mm, respectively) were virtually positioned, considering their overlapping length (~45 and ~40 mm, respectively) [16]. The axial location of the stents and the overlapping region were determined from CT images. The baseline stented SFA models (Fig. 1) were used to provide the framework the initial condition while the 1-month, 6-month and 1-year lumen geometries were used to calibrate and validate the framework.

2.2 Patient-specific multiscale framework

Figure 3 shows the fully-coupled patient-specific framework of ISR, which was adapted from the framework proposed in [7] to address the mutual interaction between hemodynamics and arterial wall

remodeling. In detail, a bi-directional coupling (previously applied in [17–19]) was here introduced to account for (i) the alteration of the hemodynamics in the remodeled vessel geometry and (ii) the subsequent cellular response (and tissue remodeling) to the updated hemodynamic condition. The framework receives as input the patient-specific stented SFA 3D geometry (i.e., post-intervention condition, Fig. 1), the blood velocity waveform and the longitudinal data of patient monocyte gene expression, and generates as output a 3D arterial lumen geometry at a specific follow-up. In particular, the framework consists of two bi-directionally coupled modules, namely (i) a hemodynamics and (ii) a tissue remodeling module.

The hemodynamics module involves the CFD meshing and simulation steps (Fig 4A), both performed in Fluent (Ansys Inc., Canonsburg, PA, USA). Specifically, the 3D stented SFA models were discretized using polyhedral elements and five boundary layers of prism elements near the wall (Fig. 4A, for the right SFA model). Curvature- and proximity-based refinements were applied with parameters obtained from a previously conducted mesh independence study [7]. Steady-state CFD simulations were performed by applying the computational settings used in [7]. In particular, as boundary conditions, (i) a parabolic velocity profile, with mean velocity derived from patient Doppler ultrasound images (0.05 and 0.07 m/s, for the left and right SFA models respectively), was prescribed at the inlet, (ii) a 0.67:0.33 flow-split was imposed at the outlets of the SFA and profunda femoris artery, respectively, and (iii) the no-slip condition was applied at the walls, considered as rigid. The blood was modeled as a non-Newtonian Carreau fluid, with density of 1060 kg/m^3. Details about the solver settings are reported in the Supplementary Materials. At the end of the CFD simulations, the wall shear stress (WSS) profile was extracted in correspondence of selected cross-sectional planes within the stented portion and used as hemodynamic driver of the ABM cellular dynamics, given its direct and endothelial-mediated influence

on smooth muscle cells (SMCs) proliferative and synthetic activity, and consequently on ISR [20]. Specifically, one plane every two stent rings, positioned approximately at the center of the stent ring, was considered, resulting in nine planes for the lesion L-A, 60 planes for the lesion L-B and 54 planes for the lesion R. Figure 4A details the WSS contour maps for the baseline stented SFA models.

The tissue remodeling module comprises the 2D ABM simulations of post-intervention arterial wall remodeling, performed in Matlab (MathWorks, Natick, MA, USA), and the 3D arterial lumen geometry reconstruction from the ABM outputs, executed in Rhinoceros (Robert McNeel & Associates, Seattle, WA, USA). A detailed description of the ABM initialization and governing rules is provided in [7]. Briefly, a three-layered arterial wall ABM structure was created for each selected cross-sectional plane (as shown in Fig. 4B for two exemplifying planes) on a 300x300 grid. The initial ABM configuration was generated based on the lumen contour and stent struts nodal coordinates of the patient-specific stented SFA model (derived from the hemodynamics module) and by setting intima, media and adventitia thicknesses of human femoral arteries, as reported in the literature [21,22]. The ABM was populated with stent strut agents, cells (i.e., SMCs) in the intima and media, and fibroblasts in the adventitia and extracellular matrix (ECM) (collagen and elastin in the intima and media, and collagen in the adventitia). Each ABM site was assumed to correspond to ~1.5 cells (SMC diameter ~25 μm [23]), thus considering a 0.0375 mm/site scale factor. Proper cell and ECM densities were set [7,17,18]. Probabilistic rules governing cell mitosis/apoptosis and ECM production/degradation were defined such that (i) baseline cellular activities were maintained in the media and adventitia layers, and (ii) the behavior of intimal cells and ECM depended on WSS- and gene expression-based inputs (*WSSinput* and *GEinput*, respectively). *WSSinput* embedded the direct and endothelial-mediated effects of WSS on SMC dynamics, according to which low WSS promotes enhanced SMC synthetic and proliferative activities

[20]. *GEinput* accounted for the patient activation state of the systemic inflammatory system due to the intervention-induced trauma along 1 post-operative month and was used to drive cellular activities, assuming that the higher *GEinput*, the more cellular activities are intensified, potentially leading to intimal hyperplasia and ISR. Thus, *WSSinput* and *GEinput* represented a local and systemic patient-specific factor for ISR, respectively. At each time-step up to 1 post-operative month, cellular activities in the intima were overall governed by *GEinput* (which equally affected all the intimal agents) and locally modulated by *WSSinput*. Following 1-month of follow-up, cellular dynamics were driven only by *WSSinput.* From that time instant, *GEinput* was assumed equal to 0 because the monocyte gene expression tended to return to the baseline pre-operative condition after 1 post-operative month. Table 1 provides the set of equations defining the formulation of the *WSSinput* and *GEinput*, and the probabilistic rules of cell mitosis/apoptosis and ECM production/degradation in the intima, media and adventitia layers. Table 2 details the list of parameters with the associated values, for those previously defined [7,17], or the admissible range, for the ones to be calibrated, as explained in Section 2.3. Further details on *WSSinput* and *GEinput* definition are reported in the Supplementary Materials.

The ABM simulation procedure followed the same initialization, agent dynamics and regularization steps described in [7]. Briefly, each agent is randomly initialized with a biological time within the agent biological cycle T_{agent} (with T_{cell}=24 hours and T_{ECM}=4 hours, for cells and ECM respectively), which is updated at each 2-hour time-step of the simulation. Within the time-step, the agents that reach the end of their biological cycle become ready to perform an event (i.e., ready to undergo cell mitosis/apoptosis or ECM production/degradation, depending on the agent type) and hence are considered as potentially active agents. Each of said agents becomes an active agent only if the occurrence of the event is verified, namely if the probability of the event (associated with the considered

agent) is greater than a randomly generated number. Consequently, the identified active agents undergo cell mitosis/apoptosis or ECM production/degradation, leading to the inclusion (in case of mitosis or ECM production) or removal (in case of apoptosis or ECM degradation) of agents within the arterial wall and the subsequent tissue reorganization. Finally, smoothing algorithms are applied to preserve a regular arterial wall structure.

To account for the ABM stochasticity, three simulations were performed for each plane [7,18]. After 1 simulated month (selected coupling period), the ABM simulations were stopped. For each plane, the output configuration among the three minimizing the root mean square deviation of the lumen contour from the average one was used to reconstruct the 3D artery lumen geometry. The lumen geometry was obtained using Rhinoceros, by lofting the lumen contour of the selected ABM output configuration for each plane. Finally, the hemodynamics – tissue remodeling modules sequence was repeated, with a coupling period of 1 month (i.e., every ABM simulated month), until the desired follow-up time of 1 year.

2.3 Framework calibration and application

The ABM parameters of the framework were calibrated using the follow-up data at 1 month and 6 months of lesion L-A. This choice was dictated by the less computational time required by the shorter lesion (nine ABM planes for lesion L-A) compared to the longer ones (60 and 54 ABM planes in the case of lesions L-B and R, respectively). The calibration procedure consisted in the following steps. First, s=60 1-month arterial configurations were generated by running the tissue remodeling module (i.e., three ABM simulations for each of the nine planes) for s=60 ABM parameter combinations of n=6 {α_2, α_3, α_5, α_6, Amp and p_{ge}} ABM parameters, as detailed in [7]. Only those n=6 ABM parameters were

considered as they were previously identified as significantly correlated with the ABM outputs through a preliminary sensitivity analysis [7]. Moreover, Latin hypercube sampling was adopted to sample the n=6 ABM parameters within their defined range (Table 2). Second, the 1-month intimal ECM/SMC ratio (ECM/SMC_{ratio_int}) normalized on the initial value was computed for each of the s=60 1-month arterial configurations, and only the configurations presenting a 1-month normalized $ECM/SMC_{ratio\_int} \in [0.5\ 1.5]$ were considered as admissible. The corresponding ABM parameter combinations were identified as admissible ABM parameter combinations, labeled as s_{adm}. The criterion on the normalized ECM/SMC_{ratio_int} represents a conservative hypothesis aimed to preserve the initial intimal ECM/cell relative content. Since the information on the patient-specific neointimal composition was not available, and changes in the ECM/cell ratio may depend on the subject and the post-procedural time [24,25], it was assumed that the ECM/cell relative content was not subjected to extreme changes over time along the remodeling process. Third, for the s_{adm} ($\leq s$) admissible ABM parameter combinations, the fully-coupled framework was run until 6-month follow-up, and s_{adm} 6-month arterial configurations were generated. Last, the optimal ABM parameter combination was identified as the one corresponding to the arterial configuration (among the s_{adm} admissible ones) associated with the minimum difference *diff* computed between the simulated and patient median lumen area of the stented portion, by considering the 1- and 6-month follow-ups, as follows:

$$diff = \left|LA_M - LA_{patient}\right|_{1M} + \left|LA_M - LA_{patient}\right|_{6M} \quad (1)$$

where LA_M and $LA_{patient}$ are the simulated and patient median lumen area of the stented portion, respectively.

Once the optimal ABM parameter combination was identified, the calibrated framework was used to simulate the post-operative arterial wall remodeling up to 1-year follow-up for the lesion L-A (i.e., along the remaining 6 months) and the lesions L-B and R (from baseline to 1-year of follow-up). The framework capability to describe and predict the long-term post-operative arterial wall remodeling was assessed by comparing the lumen geometry of the stented portion obtained from the model with that of the patient retrieved from CT imaging at 1 month, 6 months and 1 year, in terms of both lumen area (median and interquartile range) and morphology. Mann-Whitney U-test and Kruskal-Wallis test (in case of multiple comparisons) were adopted to compare the lumen area distributions (e.g., the simulated vs patient lumen area at 1-month, the patient/simulated lumen area distributions at different time points) and statistical significance was assumed for p-values < 0.05.

3. Results

3.1. Calibration

Figure 5A shows the 60 1-month arterial configurations of the lesion L-A (generated from the 60 ABM parameter combinations) in terms of distributions of lumen area of the stented portion and normalized ECM/SMC_{ratio_int}. Figure 5B highlights that 16 out of the initial 60 1-month arterial configurations (i.e., cases 2, 3, 9, 12, 17, 28, 29, 31, 32, 38, 40, 42, 46, 52, 54 and 55) satisfied the condition on the normalized $ECM/SMC_{ratio\_int} \in [0.5\ 1.5]$. These cases were considered as admissible and used to identify the optimal ABM parameter combination. Figure 5C depicts the lumen area at 1-month and 6-month follow-ups of these admissible cases, shown in ascending order according to their associated *diff* value, computed from Eq. 1. The calibration procedure identified the ABM parameter combination

#38 as the optimal one, associated with the arterial configuration that (i) best captured the 1-month and 6-month patient lumen area of the stented portion according to Eq. 1 (i.e., minimized *diff*), as shown in Fig. 5B and (ii) resulted in an admissible ECM/SMC_{ratio_int} (Table 3). The percentage difference between the simulated and patient median lumen area of the stented portion was 0.4% at month 1 and 8.5% at month 6. The optimal ABM parameters $\boldsymbol{x} = [\alpha_2, \alpha_3, \alpha_5, \alpha_6, Amp, p_{ge}]$ are reported in Table 4.

Regarding the computational resources, the calibration process required 1620 ABM simulations from baseline to 1 month (obtained by three ABM simulations for nine planes for 60 ABM parameter combinations) and 432 ABM simulations from 1 month to 6 months (obtained by three ABM simulations for nine planes for 16 ABM parameter combinations, namely the ones filtered at 1-month follow-up). Each ABM simulation took ~1 day to simulate 1 month on a single core of a computer cluster equipped with quad-core Intel Xeon CPUs E5620 at 2.40 GHz, 24 GB RAM for each node. The first set of 1620 simulations was run on 90 cores in parallel and took ~18 days, while the second set of 432 simulations was run on 72 cores in parallel and took around ~6 days per simulated month, resulting in ~30 days to complete.

3.2. Long-term application of the calibrated framework

Figures 6A, 7A and 8A show the WSS distribution in the stented portion and the temporal evolution of explanatory ABM planes (i.e., planes 1, 5 and 9 for lesion L-A, planes 10, 20, 30, 33, 42 and 51 for lesion L-B and planes 8, 16, 24, 28, 40 and 52 for the lesion R) at day 0 and month 1, 6 and 12. Moreover, Figs. 6B, 7B and 8B (for the lesions L-A, L-B and R, respectively) detail the temporal trends of the normalized lumen area and intimal SMC and ECM content of the explanatory planes (i.e., corresponding to those represented in the panel A) from baseline to 1 year, as a result of 3 repeated

simulations. Overall, no substantial differences were observed in the simulated arterial wall remodeling of the three lesions (Figs. 6, 7 and 8), although they represent distinct scenarios in terms of (i) length of the stented portion (i.e., 40 mm, 255 mm and 230 mm for the lesions L-A, L-B and R, respectively) and (ii) presence of overlapping devices in the lesions L-B and R. In all the stented lesions, the in-plane intimal growth was homogeneous and did not present highly asymmetric features. Moreover, the post-operative arterial wall remodeling obtained from the ABM simulation of each selected plane was characterized by a fast, high lumen area reduction in the first post-operative month, followed by a slowdown of the lumen narrowing over time (e.g., plane 9 of the lesion L-A, planes 10, 20, 30 and 33 of the lesion L-B, and planes 8, 24, 28 and 40 of the lesion R), or a stabilization of the lumen area in some cases (e.g., planes 1 and 5 of the lesion L-A, planes 42 and 51 of the lesion L-B and planes 16 and 52 of the lesion R), from 1-month to 1-year follow-ups. Between month 1 and month 3 a slight lumen area recovery occurred as reaction to the attenuation of the input stimuli. In particular, as observed in the intimal ECM and cell median trends (Figs. 6B, 7B and 8B, right panel), within the first post-operative month the ABM model simulates a high lumen area decrease, determined by a larger increase of the ECM content than the cellular one, while maintaining a normalized ECM/SMC_{ratio_int} within the desired range [0.5 1.5]. After 1 month, the overall perturbating stimulus drops, and a slight decrease in the intimal ECM occurs due to the propensity of the arterial system to recover the homeostatic condition, namely the physiological ECM/SMC_{ratio_int}. From month 3 the intimal ECM content re-starts growing with a growth-rate similar to the cellular one, thus preserving ECM/SMC_{ratio_int} ~1. The median 1-year lumen area reduction experienced by the displayed planes was 23%, 30% and 26% for the lesions L-A, L-B and R, respectively, with plane 9 of the lesion L-A reaching up to 31% lumen area decrease and planes 10 and 20 of the lesion L-B and plane 24 of the lesion R up to 35%. Finally, the solution of the model was

repeatable over the entire simulated period as demonstrated by the small interquartile range of the temporal trends of the normalized lumen and intima areas (Figs. 6B, 7B and 8B) and the high similarity of the outputs resulting from the three repetitions of each ABM plane at the monthly tissue remodeling – hemodynamics modules coupling (Supplementary Figs. 3-4-5).

The lumen geometry of the stented portion generated from the ABM outputs at 1 month, 6 months and 1 year was compared with the patient-specific one reconstructed from CT images at the four available follow-ups, in terms of both area (median and interquartile range) and morphology for the three lesions under investigation (Figs. 9, 10 and 11). As regards the lesion L-A, since the 1- and 6-month follow-up data were used for the calibration, the results at those specific follow-ups provided the output of the calibration process, which was in line with the expectations (Fig. 9). In particular, the framework described the significant lumen area reduction detected in the patient from baseline (Time 0) to 1-month follow-up ($p<0.05$) (Fig. 9A). Moreover, no significant differences were observed between the lumen area of the patient lumen geometry and that predicted by the framework at 1 month and 6 months (Fig. 9A). The results at 1 year allowed assessing the capability of the calibrated framework to predict the long-term arterial response to the intervention (Fig. 9). In particular, the framework successfully captured the median lumen area trend from baseline to 1 year (Fig. 9A). The lumen area change was not significantly different between 1 month and 1 year in both the patient and the model case. In addition, no significant differences were observed between the lumen area at 1 year of the patient and that predicted by the framework (Fig. 9A). However, the patient was characterized by a greater interquartile range (i.e., higher variability) of the lumen area than that of the model at all the investigated follow-ups (Fig. 9A). While the patient lumen geometries were characterized by local surface heterogeneity, with a focal restenosis detected at 1 year, the model ones were uniform (Fig. 9B). As regards the lesions L-B and R,

the application of the framework to these cases allowed evaluating the capability of the framework to predict the lumen area change from baseline to 1-year follow-up in different patient-specific cases than the one used for the calibration (Figs. 10 and 11). The framework captured the significant lumen area reduction occurring during the first post-operative month ($p<0.05$) (Figs. 10A and 11A). Moreover, the framework described the overall lumen area behavior from 1-month to 1-year follow-ups, characterized by a not-significant lumen area change after the first post-operative month (Figs. 10A and 11A). Similarly to what observed for lesion L-A, differences between the patient and the model lumen geometries were found at 1 year, due to the presence of focal lumen area reductions in the patient cases, which were not captured by the framework (Figs. 10B and 11B).

4. Discussion

The present work represents a first step towards the in-silico investigation of long-term ISR in patient-specific stented SFA arteries. The vascular adaption processes occurring in three stented SFA lesions of one patient were investigated through a multiscale computational agent-based modeling framework that integrates the effects of local hemodynamics and monocyte gene expression on cellular dynamics. Following the calibration of the driving ABM parameters based on the 1-month and 6-month follow-up data of the lesion L-A, the framework was applied to predict the lumen area change (i) from 6-month to 1-year follow-ups in a short stented SFA lesion (i.e., the lesion L-A) and (ii) from baseline to 1-year follow-up in two longer lesions of the same patient (i.e., lesions L-B and R). The framework was able to predict the overall median lumen area trend along 1 year after intervention in all the investigated lesions. Specifically, it successfully reproduced (i) the high lumen area reduction occurring

within the first post-operative month and (ii) the stabilization of the median lumen area from 1-month to 1-year follow-up. However, the spatial heterogeneity of the patient-specific arterial lumen surface and the presence of focal restenosis observable at 1-year after the intervention was not captured.

The simulated trend of the lumen area change and the lack of spatial heterogeneity in the framework outputs were consistent with the implemented mechanobiological mechanisms, the considered triggering inputs (*GEinput* and *WSSinput*) and the three main driving hypotheses, described below. First, the intervention-induced trauma was considered to be the primary factor that, through the activation of an early and intense inflammatory response (represented by *GEinput*), leads to a perturbation of the SMC activity, eventually promoting intimal hyperplasia and ISR. Second, patient monocyte gene expression data, which incorporate information on the patient systemic inflammatory activation along 1 post-operative month and were correlated with the 1-year clinical outcome, were used herein to formulate *GEinput*. Thus, *GEinput*, by uniformly influencing cellular activities, constituted a global trigger to ISR. Third, the hemodynamics, by modulating cellular activities through direct and endothelial-mediated mechanisms, constituted a local factor for ISR, which could drive heterogeneous intimal growth. Consistent with the model hypotheses: (i) the highest lumen area reduction was observed within the first post-operative month, being driven by the concurrent inflammatory and hemodynamic factors; (ii) the intimal growth experienced in the first post-operative month led to an increase in the WSS: since the arterial wall remodeling after 1-month follow-up was governed only by *WSSinput*, a subsequent slowdown of the lumen area reduction was observed after 1-month follow-up; (iii) the little spatial variability of WSS, representing the only local trigger, determined homogeneous intimal growth patterns at 1 month and beyond.

Considering all the above, the 1-year output of the model suggests that the local events leading to the patient focal restenosis at 1-year follow-up are most likely related to several factors that are not accounted by the present framework, such as patient comorbidities, lesion-specific features, procedural characteristics, progression of the atherosclerotic disease, rather than the sole local hemodynamics [26]. In detail, the patient lumen geometries at 6-month follow-up are quite uniform and similar to those obtained using the framework. Thus, it is reasonable that at that time instant the patient lumen WSS distribution is quite homogenous. This means that in the time period between 6 months and 1 year some phenomena (not related to the WSS magnitude) activate in all the patient lesions. Furthermore, it should be noted that the three analyzed SFA lesions represent different scenarios, namely a short (i.e., 40-mm) lesion treated with a single device (lesion L-A) and long (i.e., 250-mm and 230-mm) lesions treated with two overlapping stents (lesions L-B and R). Hence, the factors promoting the focal events at 1 year in these cases are probably not related neither to the lesion length nor to the presence of overlapping stents. Moreover, the patient under investigation did not present either coronary artery disease nor diabetes, thus excluding the role of said comorbidities in fostering ISR [26]. Although based on the analysis of only three SFA lesions, this further confirms that the complex interplay of different, heterogeneous events likely determines the intervention outcome after 6 months follow-up.

Intravascular imaging modalities allows detecting the arterial wall composition [27] and might be crucial to gain insights into the ISR process. Besides providing information on the baseline lesion tissue composition and plaque features potentially determining local heterogeneous responses to the intervention, details on the post-intervention arterial tissue changes would suggest whether phenomena of neoatherosclerosis (i.e., de novo in-stent atherosclerotic plaque development) or paleoatherosclerosis (i.e., progression of pre-existing plaque) occur or not [28]. These phenomena have recently gained

interest and have been associated to the occurrence of late lumen area reduction (responsible for the third phase of the lumen area trajectory) in coronary arteries [28,29]. Nevertheless, similar investigations in the femoral arteries are lacking, probably due to the limited application of intravascular imaging modalities in this vascular region. In-stent atherosclerosis might explain the three-phase lumen area change and the 1-year focal restenosis occurring in the stented SFAs analyzed herein.

In this work, given the unavailability of patient data on the lesion arterial wall tissue composition and its evolution during the post-operative period, and based on the absence of a clear evident pattern in literature studies, a constraint on the normalized ECM/SMC_{ratio_int} was assumed. According to this constrain, the baseline ratio between ECM and SMC components in the intima tends to be preserved throughout the restenosis process. Interestingly, while maintaining the normalized ECM/SMC_{ratio_int} within the admissible range$\in[0.5\ 1.5]$, the model simulates an overall increase in both the SMC and ECM contents from baseline to 1-year follow-up but with a different trend. While the SMC content undergoes a monotonic increase, the ECM content trend is characterized by the following three phases: (i) increase with a growth-rate greater than that of SMCs in the first post-operative month, leading to an increase of the ECM/SMC_{ratio_int}, (ii) slight decrease between month 1 and month 3 up to approaching the SMC trend and restoring the baseline $ECM/SMC_{ratio\_int,}$ and (iii) final increase with a growth-rate similar to that of SMCs, thus preserving the ECM/SMC_{ratio_int}. Although in this work the simulated behavior of cells and ECM content was not controlled (with the exception of the constrained on the normalized ECM/SMC_{ratio_int}), these results show the potentiality of the model to describe a possible pattern of the tissue composition evolution throughout the restenosis process, which, in this case was driven by the tendency of the model to restore the physiological condition. Given the role that the evolution of the

lesion tissue composition likely plays in deciphering the underlying mechanisms of ISR progression, the calibration of said dynamics is thought to markedly improve the predictive power of the framework.

To identify the optimal combination of ABM parameters, a calibration procedure was performed on the short lesion (i.e., lesion L-A). The choice of this lesion instead of the longer ones was motivated by the computational effort required for the calibration process. To the authors' opinion, the choice of a different lesion for the calibration would have not substantially changed the overall model performance, and, in particular would have not provided a better result at 1-year follow-up, in terms of capability to predict focal restenosis. Indeed, the patient median lumen area trend up to 6 months is similar in all the three lesions, being characterized by a reduction within the first post-operative month (i.e., ~25%, ~18% and ~16% in the lesions L-A, L-B and R, respectively) and a slight increase between 1 month and 6 months (i.e., ~7%, ~2% and ~4% in the lesions L-A, L-B and R, respectively).

The study is limited by the number of investigated SFA lesions. Nevertheless, thanks to the novelty and potentialities emerged from this analysis, the proposed framework lays the basis for future studies aimed at deciphering the mechanobiological mechanisms underlying arterial wall remodeling following endovascular procedures. In particular, future investigations of the triggering events and processes driving late focal restenosis is of primary relevance. To this aim, the availability of data on arterial wall tissue composition evolution is thought to be crucial, as well as the application of the framework to a larger cohort of patient cases (including patients from both success and failure groups).

5. Conclusions

The developed patient-specific multiscale computational agent-based modeling framework of ISR, by integrating the effects of local hemodynamics and monocyte gene expression on cellular activity, simulated the short-term and long-term arterial wall remodeling following stent deployment intervention in three stented SFA lesions. The framework provided an excellent estimation of the lumen area reduction from baseline to 1-month follow-up and well captured the median lumen area trajectory along 1-year. The limited capability to describe the spatial heterogeneity of the lumen and to predict the focal restenosis at 1-year follow-up highlighted the importance of including additional local factors contributing to the arterial wall remodeling in future investigations. In this context, the availability of different types of patient-specific data, such as the evolution of tissue composition over the follow-up period, is thought to be fundamental for the implementation of other mechanobiological mechanisms potentially driving late ISR.

Declarations

Author Contributions

A.C.: conceptualization, data curation, formal analysis, investigation, methodology, software, validation, visualization, writing – original draft, writing – review & editing; F.M.: resources, writing – review & editing; S.A.B.: data curation, writing – review & editing; C.C.: conceptualization, methodology, funding acquisition, supervision, funding acquisition, writing – original draft, writing – review & editing.

Data Accessibility

The input data used to set up the computational framework are available from previous studies. In particular, gene expression data were derived from the study of DeSart et al. J. Vasc. Surg. 2016 [11]. Gene expression analysis was based on the study of Wang et al. Brief. Bioinform. 2012 (doi:10.1093/bib/bbr032). The patient-specific vessel geometry was reconstructed from the study of Colombo et al. Ann. Biomed. Eng. 2021 [12]. The computational framework is exhaustively described in the methods of the manuscript and the electronic supplementary materials, as well as in our previous publications [7,17,18].

In addition, the post-prints of previous publications are freely available in Zenodo, since were part of a funded project requiring accessibility of the publications: Corti A et al. 2020 Comput. Biol. Med. [17] (https://zenodo.org/record/3629400#.Y-UujC-ZO5c); Corti A et al. 2022 J. R. Soc. Interface [7] (https://zenodo.org/record/6400685#.Y-Uu1i-ZO5c).

The description enables the reproducibility of the framework.

Ethics

This study was approved by the Institutional Review Board at the University of Florida and conformed to the Helsinki Declaration on human research of 1975, as revised in 2000. Written informed consent was obtained from the patients. No animal studies were carried out by the authors for this article.

Funding Statement

This work has been partially supported by Fondazione Cariplo, Italy (Grant number 2017-0792, TIME). FM and CC have been also partially supported by the Italian Ministry of Education, University and Research (FISR2019_03221, CECOMES).

Competing interests

The authors declare that they have no competing interests.

References

1. Criqui MH, Matsushita K, Aboyans V, Hess CN, Hicks CW, Kwan TW, McDermott MM, Misra S, Ujueta F. 2021 Lower Extremity Peripheral Artery Disease: Contemporary Epidemiology, Management Gaps, and Future Directions: A Scientific Statement From the American Heart Association. *Circulation* **144**, e171–e191. (doi:10.1161/CIR.0000000000001005)

2. Kasapis C, Gurm HS. 2010 Current approach to the diagnosis and treatment of femoral-popliteal arterial disease. A systematic review. *Curr. Cardiol. Rev.* **5**, 296–311. (doi:10.2174/157340309789317823)

3. Katsanos K, Tepe G, Tsetis D, Fanelli F. 2014 Standards of practice for superficial femoral and popliteal artery angioplasty and stenting. *Cardiovasc. Intervent. Radiol.* **37**, 592–603.

(doi:10.1007/s00270-014-0876-3)

4. Kim W, Choi D. 2018 Treatment of femoropopliteal artery in-stent restenosis. *Korean Circ. J.* **48**, 191–197. (doi:10.4070/kcj.2018.0074)

5. Chaabane C, Otsuka F, Virmani R, Bochaton-Piallat ML. 2013 Biological responses in stented arteries. *Cardiovasc. Res.* **99**, 353–363. (doi:10.1093/cvr/cvt115)

6. Corti A, Colombo M, Migliavacca F, Rodriguez Matas JF, Casarin S, Chiastra C. 2021 Multiscale Computational Modeling of Vascular Adaptation: A Systems Biology Approach Using Agent-Based Models. *Front. Bioeng. Biotechnol.* **9**, 744560. (doi:10.3389/fbioe.2021.744560)

7. Corti A *et al.* 2022 A predictive multiscale model of in-stent restenosis in femoral arteries: linking hemodynamics and gene expression with an agent-based model of cellular dynamics. *J. R. Soc. Interface* , 20210871. (doi:https://doi.org/10.1098/rsif.2021.0871)

8. Schillinger M, Exner M, Mlekusch W, Rumpold H, Ahmadi R, Sabeti S, Haumer M, Wagner O, Minar E. 2002 Vascular inflammation and percutaneous transluminal angioplasty of the femoropopliteal artery: association with restenosis. *Radiology* **225**, 21–26. (doi:10.1148/radiol.2251011809)

9. Schillinger M, Exner M, Mlekusch W, Haumer M, Ahmadi R, Rumpold H, Wagner O, Minar E. 2002 Balloon angioplasty and stent implantation induce a vascular inflammatory reaction. *J. Endovasc. Ther. an Off. J. Int. Soc. Endovasc. Spec.* **9**, 59–66. (doi:10.1177/152660280200900111)

10. Cipollone F *et al.* 2001 Elevated circulating levels of monocyte chemoattractant protein-1 in

patients with restenosis after coronary angioplasty. *Arterioscler. Thromb. Vasc. Biol.* **21**, 327–334. (doi:10.1161/01.ATV.21.3.327)

11. DeSart K, O'Malley K, Schmit B, Lopez MC, Moldawer L, Baker H, Berceli S, Nelson P. 2016 Systemic inflammation as a predictor of clinical outcomes after lower extremity angioplasty/stenting. *J. Vasc. Surg.* **64**, 766-778.e5. (doi:10.1016/j.jvs.2015.04.399)

12. Colombo M *et al.* 2021 In-Stent Restenosis Progression in Human Superficial Femoral Arteries: Dynamics of Lumen Remodeling and Impact of Local Hemodynamics. *Ann. Biomed. Eng.* **49**, 2349–2364. (doi:10.1007/s10439-021-02776-1)

13. Iida O *et al.* 2011 Timing of the restenosis following nitinol stenting in the superficial femoral artery and the factors associated with early and late restenoses. *Catheter. Cardiovasc. Interv. Off. J. Soc. Card. Angiogr. Interv.* **78**, 611–617. (doi:10.1002/ccd.23064)

14. Wang Y, Xu M, Wang Z, Tao M, Zhu J, Wang L, Li R, Berceli SA, Wu R. 2012 How to cluster gene expression dynamics in response to environmental signals. *Brief. Bioinform.* **13**, 162–174. (doi:10.1093/bib/bbr032)

15. Colombo M, Bologna M, Garbey M, Berceli S, He Y, Rodriguez Matas JF, Migliavacca F, Chiastra C. 2020 Computing patient-specific hemodynamics in stented femoral artery models obtained from computed tomography using a validated 3D reconstruction method. *Med. Eng. Phys.* **75**, 23–35. (doi:10.1016/j.medengphy.2019.10.005)

16. Colombo M *et al.* 2022 Superficial femoral artery stenting: Impact of stent design and overlapping on the local hemodynamics. *Comput. Biol. Med.* , 105248.

(doi:https://doi.org/10.1016/j.compbiomed.2022.105248)

17. Corti A, Chiastra C, Colombo M, Garbey M, Migliavacca F, Casarin S. 2020 A fully coupled computational fluid dynamics – agent-based model of atherosclerotic plaque development: Multiscale modeling framework and parameter sensitivity analysis. *Comput. Biol. Med.* **118**, 103623. (doi:10.1016/j.compbiomed.2020.103623)

18. Corti A, Colombo M, Migliavacca F, Berceli SA, Casarin S, Rodriguez Matas JF, Chiastra C. 2022 Multiscale agent-based modeling of restenosis after percutaneous transluminal angioplasty: Effects of tissue damage and hemodynamics on cellular activity. *Comput. Biol. Med.* **147**, 105753. (doi:10.1016/j.compbiomed.2022.105753)

19. Corti A, Casarin S, Chiastra C, Colombo M, Migliavacca F, Garbey M. 2019 A Multiscale Model of Atherosclerotic Plaque Development: Toward a Coupling Between an Agent-Based Model and CFD Simulations. In *Computational Science -- ICCS 2019* (eds JMF Rodrigues, PJS Cardoso, J Monteiro, R Lam, V V Krzhizhanovskaya, MH Lees, JJ Dongarra, PMA Sloot), pp. 410–423. Cham: Springer International Publishing.

20. Koskinas KC, Chatzizisis YS, Antoniadis AP, Giannoglou GD. 2012 Role of endothelial shear stress in stent restenosis and thrombosis: Pathophysiologic mechanisms and implications for clinical translation. *J. Am. Coll. Cardiol.* **59**, 1337–1349. (doi:10.1016/j.jacc.2011.10.903)

21. Hafner NM, Womack CJ, Luden ND, Todd MK. 2016 Arterial adaptations to training among first time marathoners. *Cardiovasc. Ultrasound* **14**, 1–9. (doi:10.1186/s12947-016-0063-6)

22. Wong M, Edelstein J, Wollman J, Bond MG. 1993 Ultrasonic-pathological comparison of the

human arterial wall. Verification of intima-media thickness. *Arterioscler. Thromb. A J. Vasc. Biol.* **13**, 482–486. (doi:10.1161/01.ATV.13.4.482)

23. Tahir H, Niculescu I, Bona-Casas C, Merks RMH, Hoekstra AG. 2015 An in silico study on the role of smooth muscle cell migration in neointimal formation after coronary stenting. *J. R. Soc. Interface* **12**, 20150358. (doi:10.1098/rsif.2015.0358)

24. Chung IM, Gold HK, Schwartz SM, Ikari Y, Reidy MA, Wight TN. 2002 Enhanced extracellular matrix accumulation in restenosis of coronary arteries after stent deployment. *J. Am. Coll. Cardiol.* **40**, 2072–2081. (doi:10.1016/S0735-1097(02)02598-6)

25. Kearney M, Pieczek A, Haley L, Losordo DW, Andres V, Schainfeld R, Rosenfield K, Isner JM. 1997 Histopathology of in-stent restenosis in patients with peripheral artery disease. *Circulation* **95**, 1998–2002. (doi:10.1161/01.CIR.95.8.1998)

26. Buccheri D, Piraino D, Andolina G, Cortese B. 2016 Understanding and managing in-stent restenosis: A review of clinical data, from pathogenesis to treatment. *J. Thorac. Dis.* **8**, E1150–E1162. (doi:10.21037/jtd.2016.10.93)

27. Ramasamy A *et al.* 2019 Reliable in vivo intravascular imaging plaque characterization: A challenge unmet. *Am. Heart J.* **218**, 20–31. (doi:10.1016/j.ahj.2019.07.008)

28. Andreou I, Stone PH, Ikonomidis I, Alexopoulos D, Sabaté M. 2020 Recurrent atherosclerosis complications as a mechanism for stent failure. *Hellenic J. Cardiol.* **61**, 9–14. (doi:10.1016/j.hjc.2019.04.007)

29. Otsuka F *et al.* 2015 Neoatherosclerosis: overview of histopathologic findings and implications

for intravascular imaging assessment. *Eur. Heart J.* **36**, 2147–2159. (doi:10.1093/eurheartj/ehv205)

Table captions

Table 1. Agent-based model inputs and cellular activities.

Table 2. Agent-based model parameters.

Table 3. Details on the patient lumen area and on the lumen area and normalized intimal extracellular matrix / smooth muscle cell ratio (ECM/SMC_{ratio_int}) obtained with the agent-based model (ABM) parameter combinations #38.

Table 4. Calibrated agent-based model parameters.

Figures

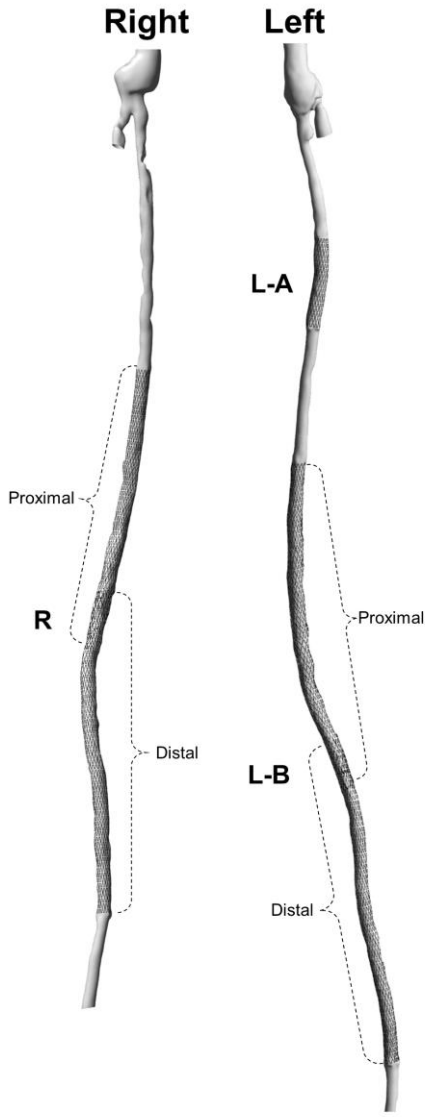

Figure 1. Patient-specific models of the right and left superficial femoral arteries (SFAs) treated with EverFlex stents at the Malcom Randall VA Medical Center (Gainesville, FL, USA). The regions delimited by the proximal and distal stents in lesions R and L-B are indicated.

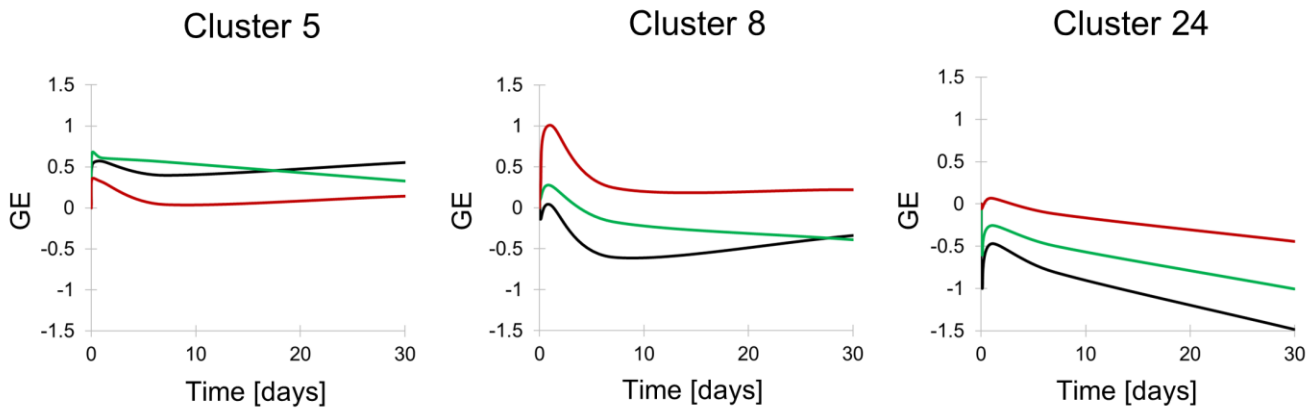

Figure 2. Gene expression (GE) of the 3 clusters presenting with significant differential expression between success and failure groups. For each cluster i) the black curve is the average curve of the patient expression profiles of the genes belonging to the cluster ii) the green curve represents the average curve for all the patients belonging success group (i.e., average of the expression profiles of the cluster genes of all the success patients) and iii) the red curve represents the average curve for all the patients belonging failure group (i.e., average of the expression profiles of the cluster genes of all the failure patients). All the gene expression curves were $\log_2$-transformed, namely the displayed value of gene expression was computed as $GE(t) = log_2\left(\frac{v(t)}{v(t0)}\right)$, where *v(t)* is the measured gene expression level at time *t* and *v(t0)* is the pre-operative gene expression level.

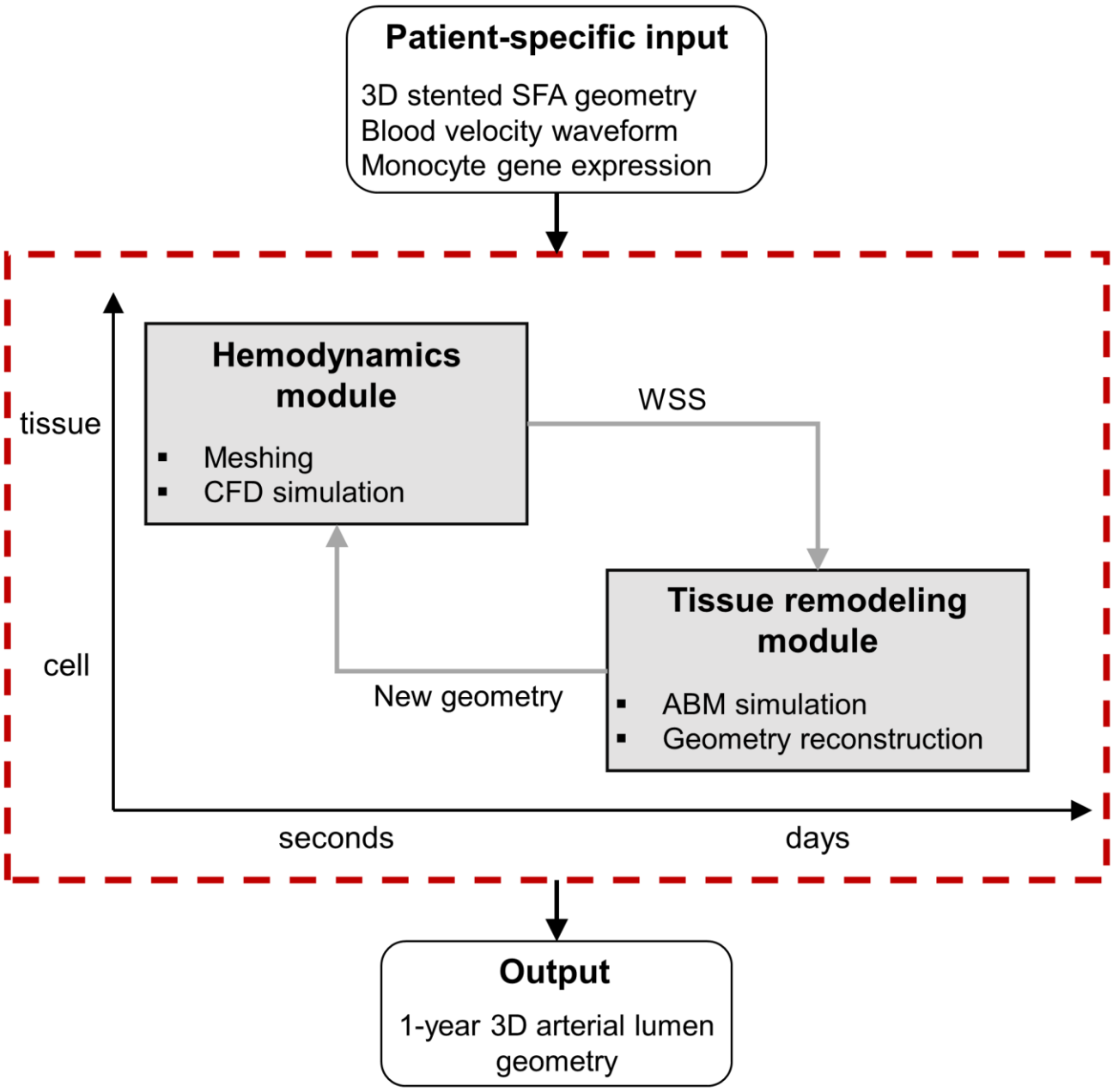

Figure 3. Multiscale computational agent-based modeling framework. Starting from the patient-specific inputs, the framework (dashed red box) simulates arterial wall remodeling and in-stent restenosis (ISR) along 1 year and generates as output a three-dimensional (3D) model of arterial lumen geometry at 1-year follow-up. The framework consists of two bidirectionally coupled modules, namely (i) the

hemodynamics module at the tissue-seconds scale, in which the 3D artery model is meshed and the computational fluid dynamics (CFD) simulation is performed to compute the wall shear stress (WSS), and (ii) the tissue remodeling module at the cell-days scale, in which an agent-based model (ABM) simulates cellular dynamics and arterial wall remodeling, and an updated 3D arterial lumen geometry is reconstructed from the ABM outputs.

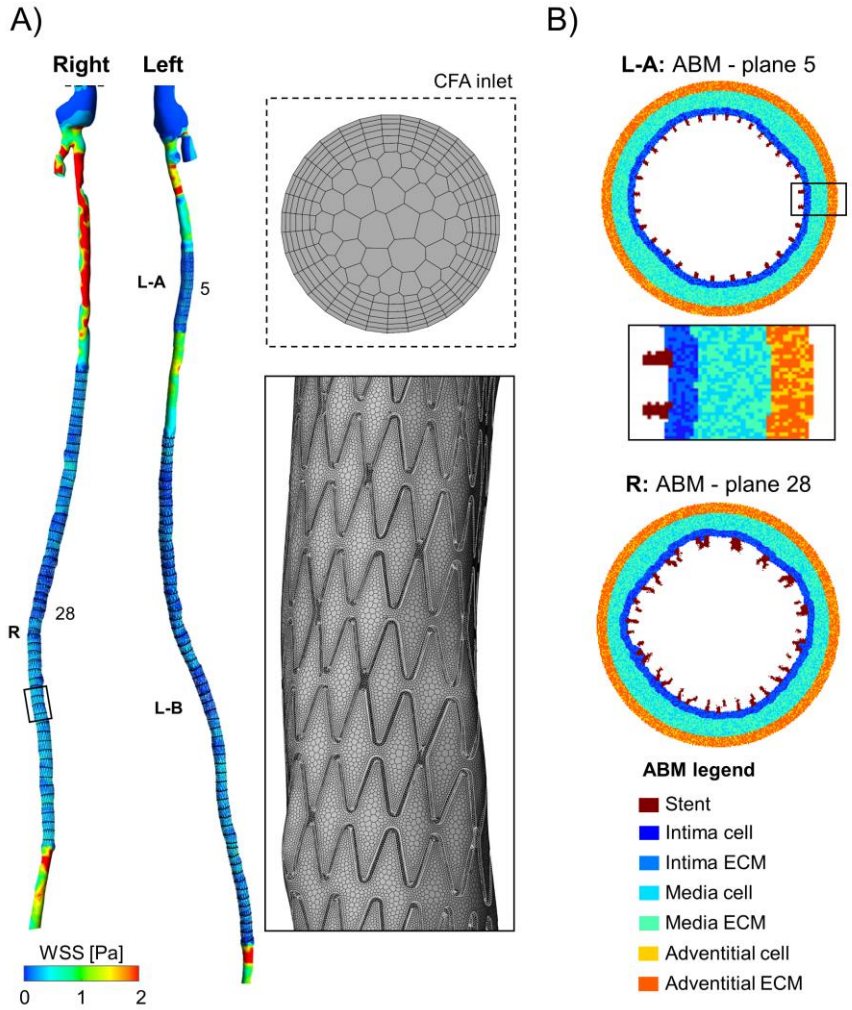

Figure 4. A) Wall shear stress (WSS) contour maps resulting from the computational fluid dynamics (CFD) simulations in the left and right superficial femoral artery (SFA) models. In the stented portions, cross-sectional planes were selected (1 every 2 stent rings) for the subsequent agent-based analysis (9 planes for the lesion L-A, 60 planes for the lesion L-B and 54 planes for the lesion R). Detail of the polyhedral CFD mesh of the common femoral artery (CFA) inlet and stented portion of the right SFA model. B) Agent-based models (ABM) of plane 5 of the lesion L-A (with a magnification on a portion

of the arterial wall) and plane 28 of the lesion R (within the overlapping region). Overlapped stent struts can be observed in plane 28.

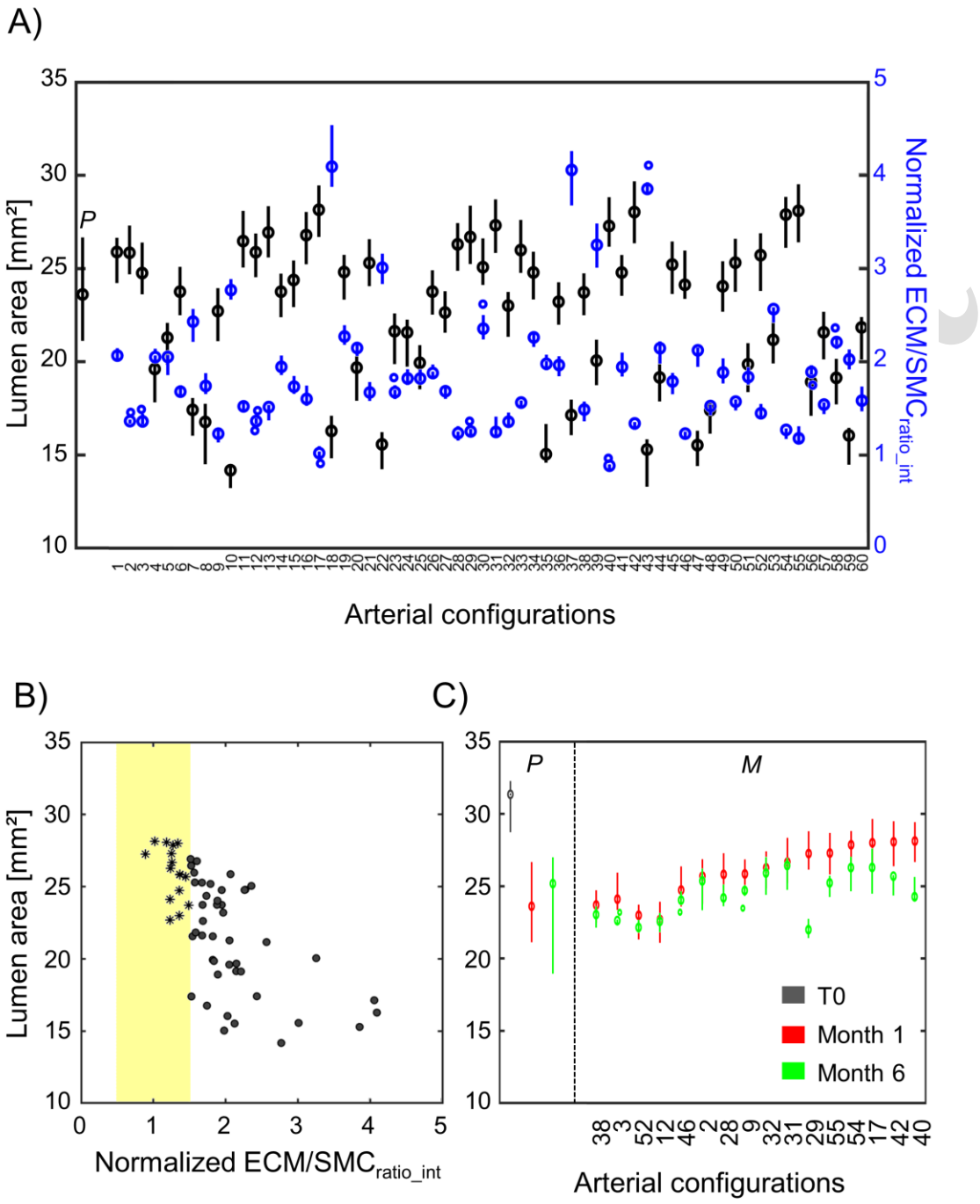

Figure 5. A) 60 1-month arterial configurations of the lesion L-A, which were obtained running the framework. The grey box plots represent the distribution of the 1-month lumen area of the stented portion

of the patient (*P*, first box plot) and of the 60 arterial configurations obtained from the model. The blue box plots represent the distributions of the 1-month normalized intimal extracellular matrix / smooth muscle cell ratio (ECM/SMC_{ratio_int}) of the 60 arterial configurations obtained from the model. B) Scatterplot of the lumen area vs. normalized ECM/SMC_{ratio_int} for the 60 1-month arterial configurations of the lesion L-A obtained from the model (for each configuration, the median value over three repetitions was considered). The asterisks represent the s_{adm} = 16 admissible arterial configurations, presenting with the 1-month normalized $ECM/SMC_{ratio\_int} \in [0.5\ 1.5]$ (range identified through the yellow band), while the circles represent the remaining 44 configurations. C) Left portion: patient lumen area of the stented portion at baseline (T0, grey), 1 month (red) and 6 months (green); Right portion: lumen area at 1-month (red) and 6-month (green) follow-ups of the s_{adm} = 16 admissible arterial configurations out of the initial 60 1-month configurations of the lesion L-A presenting with the 1-month normalized $ECM/SMC_{ratio\_int} \in [0.5\ 1.5]$. The s_{adm} cases are shown in ascending order according to their associated *diff* value, computed from Eq. 1. P: patient; M: model.

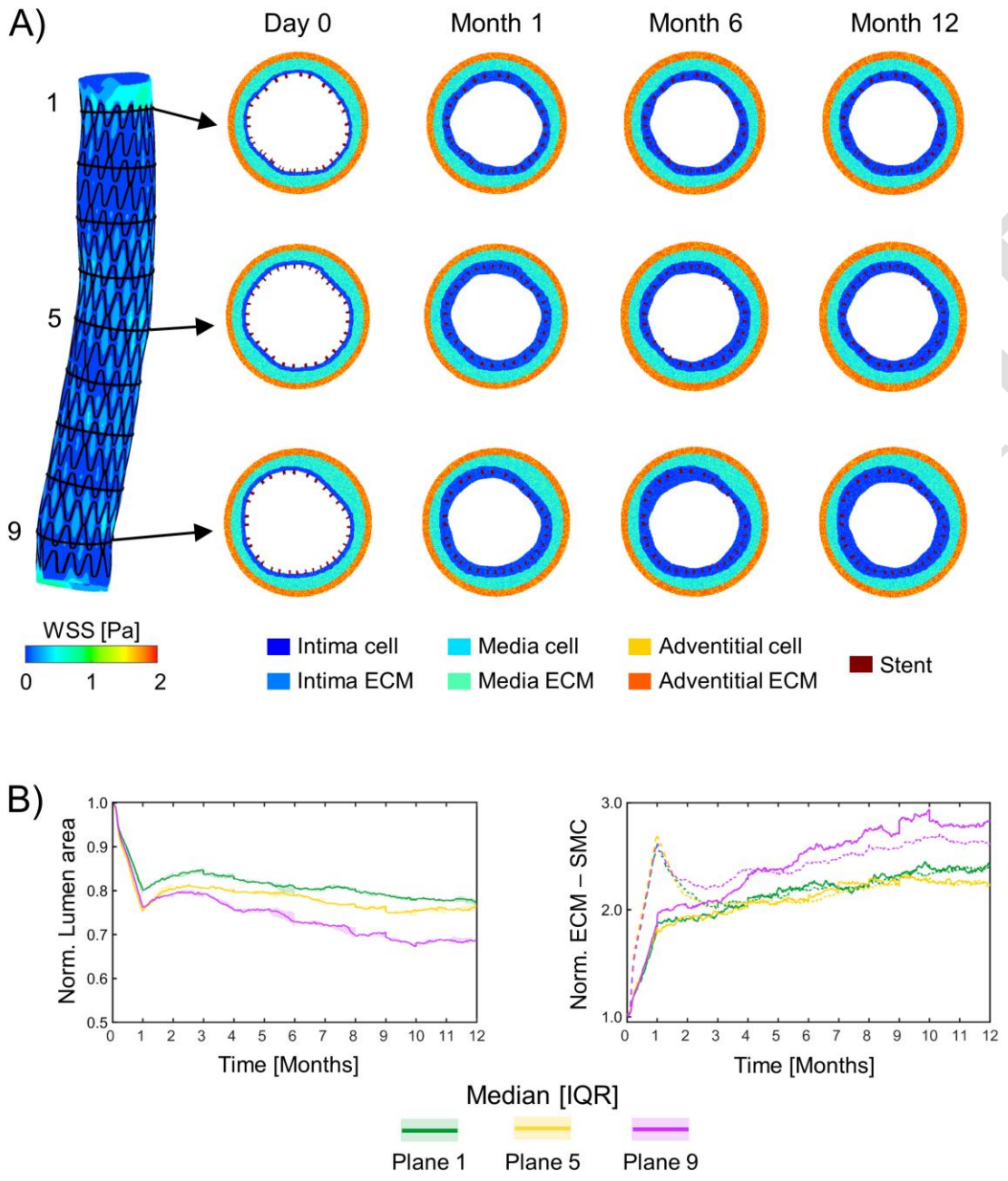

Figure 6. Results of the calibrated framework for three explanatory planes of the left proximal stented superficial femoral artery lesion (lesion L-A). A) Color map of wall shear stress (WSS) of the stented portion (left) and temporal evolution of the agent-based models (ABM) of three explanatory planes

(planes 1, 5 and 9) at day 0 and month 1, 6 and 12. For each ABM plane, the results were retrieved from one out of three ABM simulations, namely the one presenting the lumen configuration minimizing the root mean square deviation from the average one. B) Normalized lumen area over time (median and interquartile range) for planes 1 (green), 5 (yellow) and 9 (violet) from baseline to 12 simulated months. C) Normalized extracellular matrix (ECM) and smooth muscle cell (SMC) intimal content over time (dashed and solid lines, respectively) for planes 1 (green), 5 (yellow) and 9 (violet) from baseline to 12 simulated months.

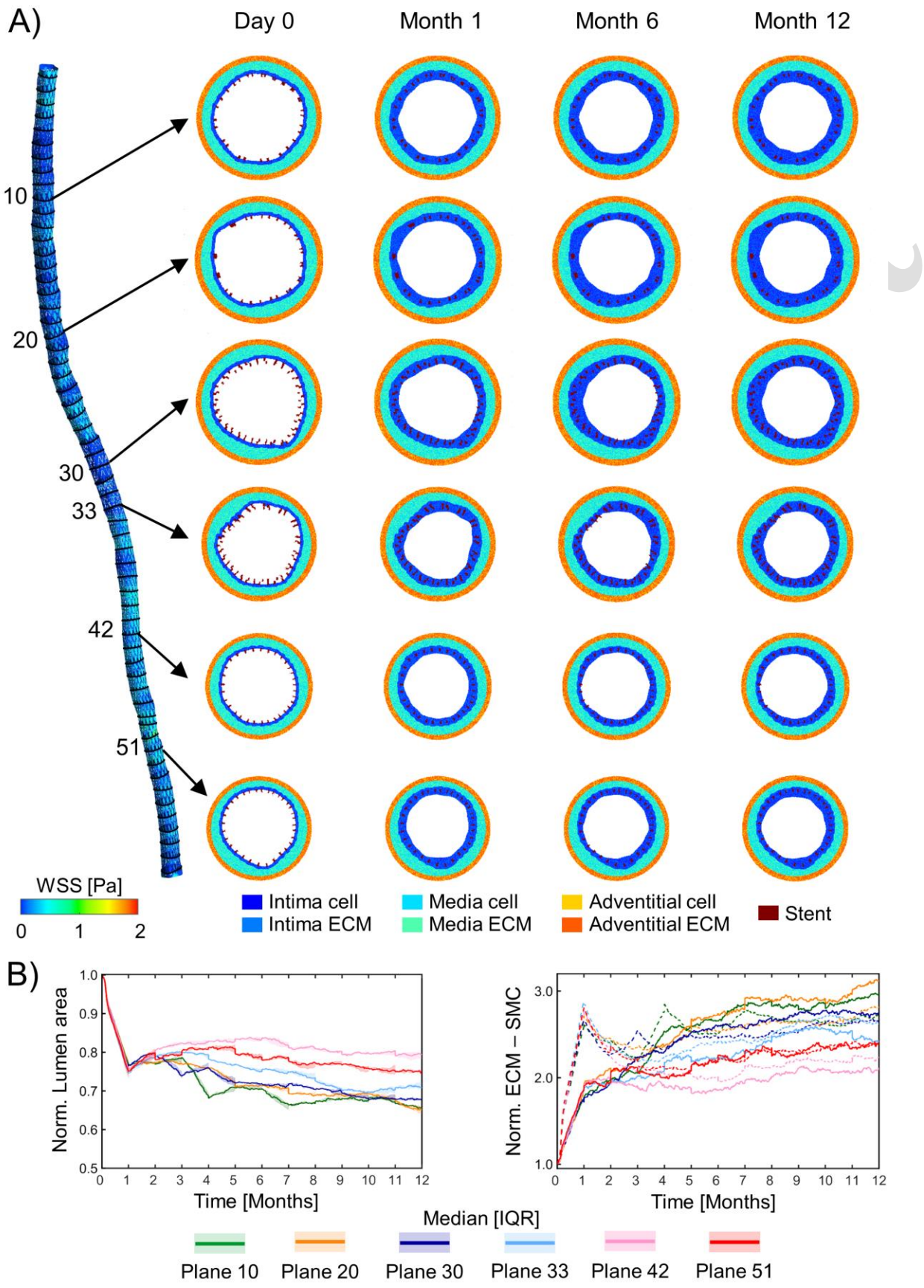
A)
Day 0
Month 1
Month 6
Month 12
10
20
30
33
42
51
WSS [Pa]
0
1
2
Intima cell
Intima ECM
Media cell
Media ECM
Adventitial cell
Adventitial ECM
Stent
B)
Norm. Lumen area
Time [Months]
Norm. ECM – SMC
Time [Months]
Median [IQR]
Plane 10
Plane 20
Plane 30
Plane 33
Plane 42
Plane 51

Figure 7. Results of the calibrated framework for six explanatory planes of the left distal stented superficial femoral artery lesion (lesion L-B). A) Color map of wall shear stress (WSS) of the stented portion (left) and temporal evolution of the agent-based models (ABM) of six explanatory planes (planes 10, 20, 30, 33, 42 and 51) at day 0 and month 1, 6 and 12. For each ABM plane, the results were retrieved from one out of three ABM simulations, namely the one presenting the lumen configuration minimizing the root mean square deviation from the average one. B) Normalized lumen area over time (median and interquartile range) for planes 10 (green), 20 (orange), 30 (blue), 33 (light blue), 42 (pink) and 51 (red) from baseline to 12 simulated months. C) Normalized extracellular matrix (ECM) and smooth muscle cell (SMC) intimal content over time (dashed and solid lines, respectively) for planes 10 (green), 20 (orange), 30 (blue), 33 (light blue), 42 (pink) and 51 (red) from baseline to 12 simulated months.

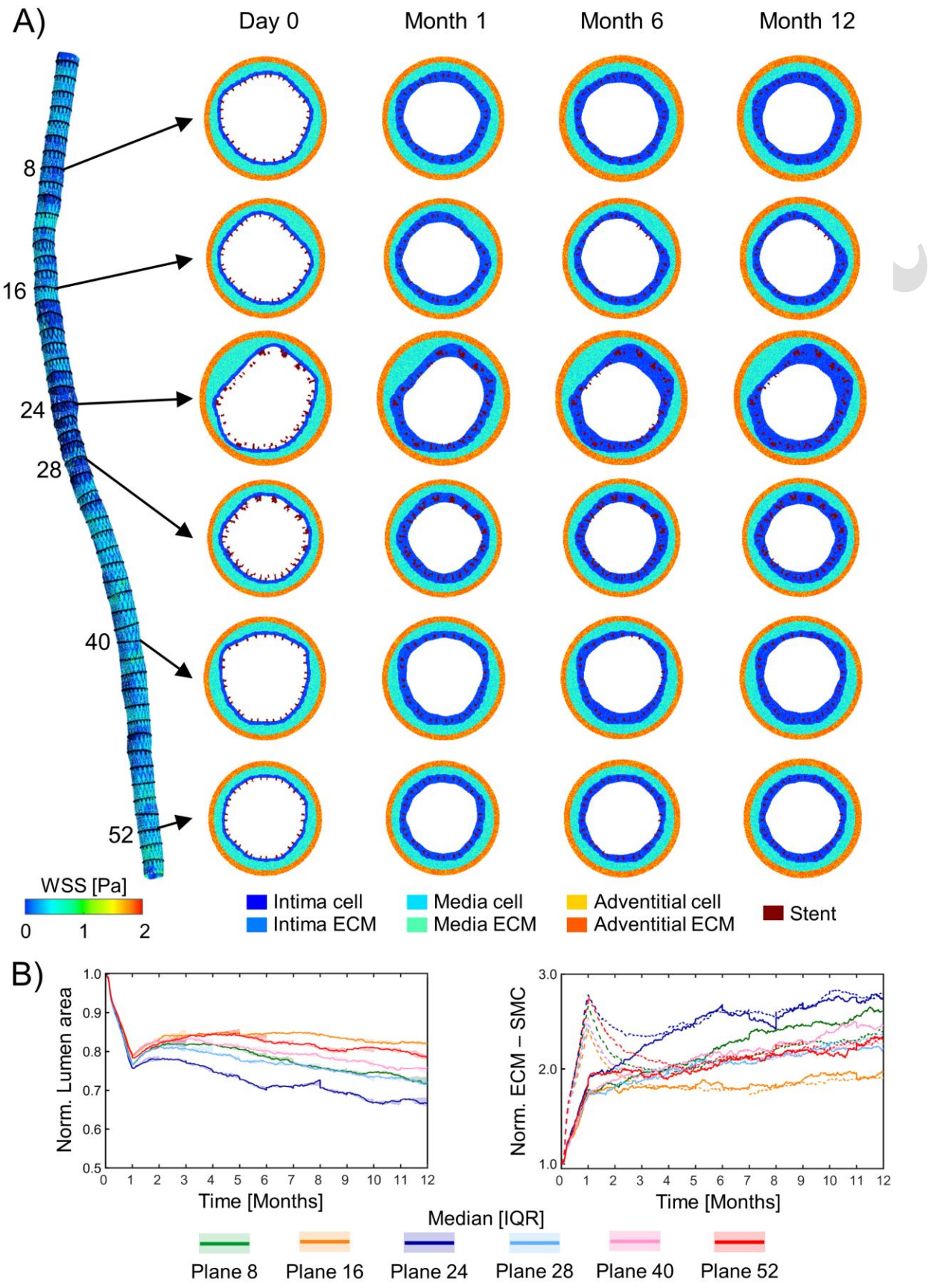
A)
Day 0
Month 1
Month 6
Month 12
8
16
24
28
40
52
WSS [Pa]
0
1
2
Intima cell
Intima ECM
Media cell
Media ECM
Adventitial cell
Adventitial ECM
Stent
B)
Norm. Lumen area
Time [Months]
Norm. ECM – SMC
Time [Months]
Median [IQR]
Plane 8
Plane 16
Plane 24
Plane 28
Plane 40
Plane 52

Figure 8. Results of the calibrated framework for six explanatory planes of the right stented superficial femoral artery lesion (lesion R). A) Color map of wall shear stress (WSS) of the stented portion (left) and temporal evolution of the agent-based models (ABM) of six explanatory planes (planes 8, 16, 24, 28, 40 and 52) at day 0 and month 1, 6 and 12. For each ABM plane, the results were retrieved from one out of three ABM simulations, namely the one presenting the lumen configuration minimizing the root mean square deviation from the average one. B) Normalized lumen area over time (median and interquartile range) for planes 8 (green), 16 (orange), 24 (blue), 28 (light blue), 40 (pink) and 52 (red) from baseline to 12 simulated months. C) Normalized extracellular matrix (ECM) and smooth muscle cell (SMC) intimal content over time (dashed and solid lines, respectively) for planes 8 (green), 16 (orange), 24 (blue), 28 (light blue), 40 (pink) and 52 (red) from baseline to 12 simulated months.

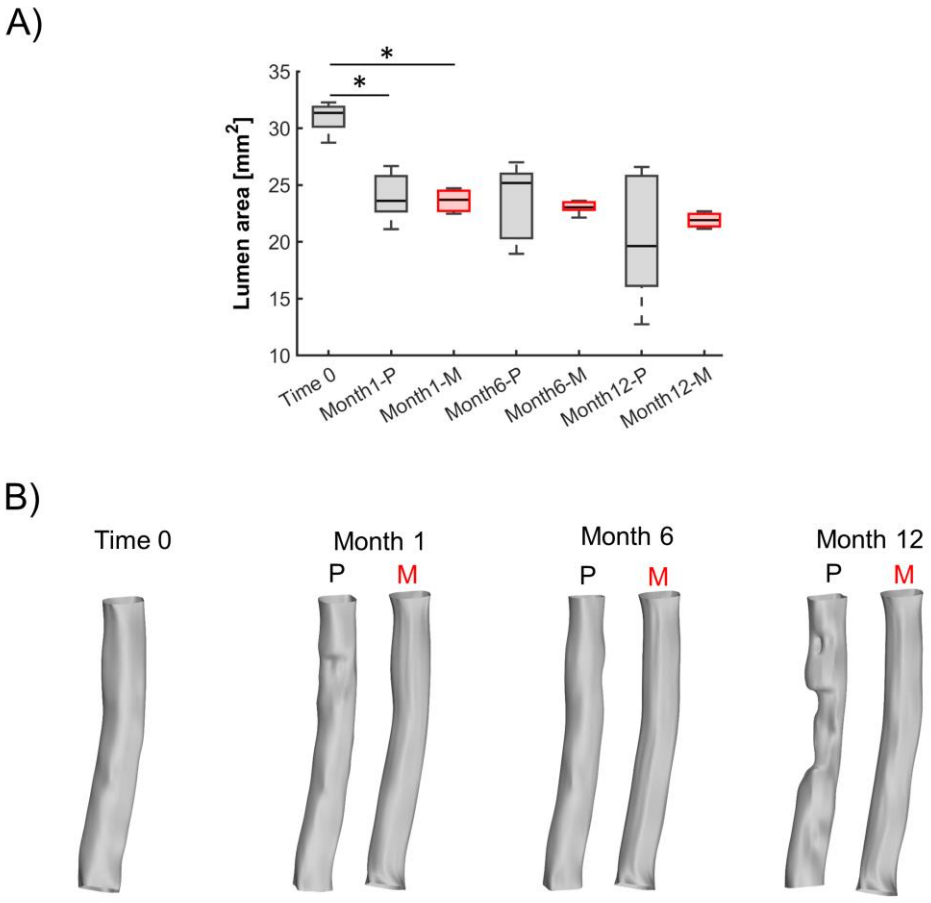

Figure 9. Evaluation of the calibrated framework applied to the left proximal stented superficial femoral artery lesion (lesion L-A). A) Boxplots of the lumen area of the stented portion immediately after the intervention (Time 0), at month 1 of the patient case (Month1-P) and of the calibrated model case (Month1-M), at month 6 of the patient case (Month6-P) and of the calibrated model case (Month6-M), and at month 12 of the patient case (Month12-P) and of the calibrated model case (Month12-M). Mann-Whitney U-test was used for pairwise comparisons. *p-value < 0.05. B) Comparison between the lumen geometries of the stented portion of the patient (reconstructed from computer tomography at the four available follow-ups), denoted as P, and of the calibrated model (generated from the ABM outputs at 1 month, 6 months and 12 months), denoted as M.

A)

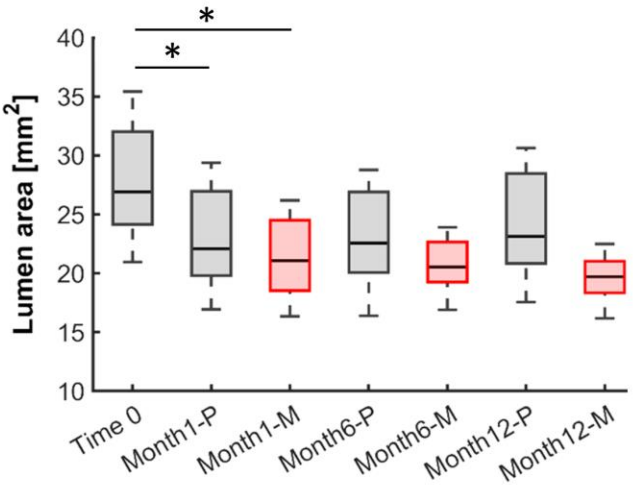
*
*
40
35
30
25
20
15
10
Lumen area [mm²]
Time 0
Month1-P
Month1-M
Month6-P
Month6-M
Month12-P
Month12-M

B)

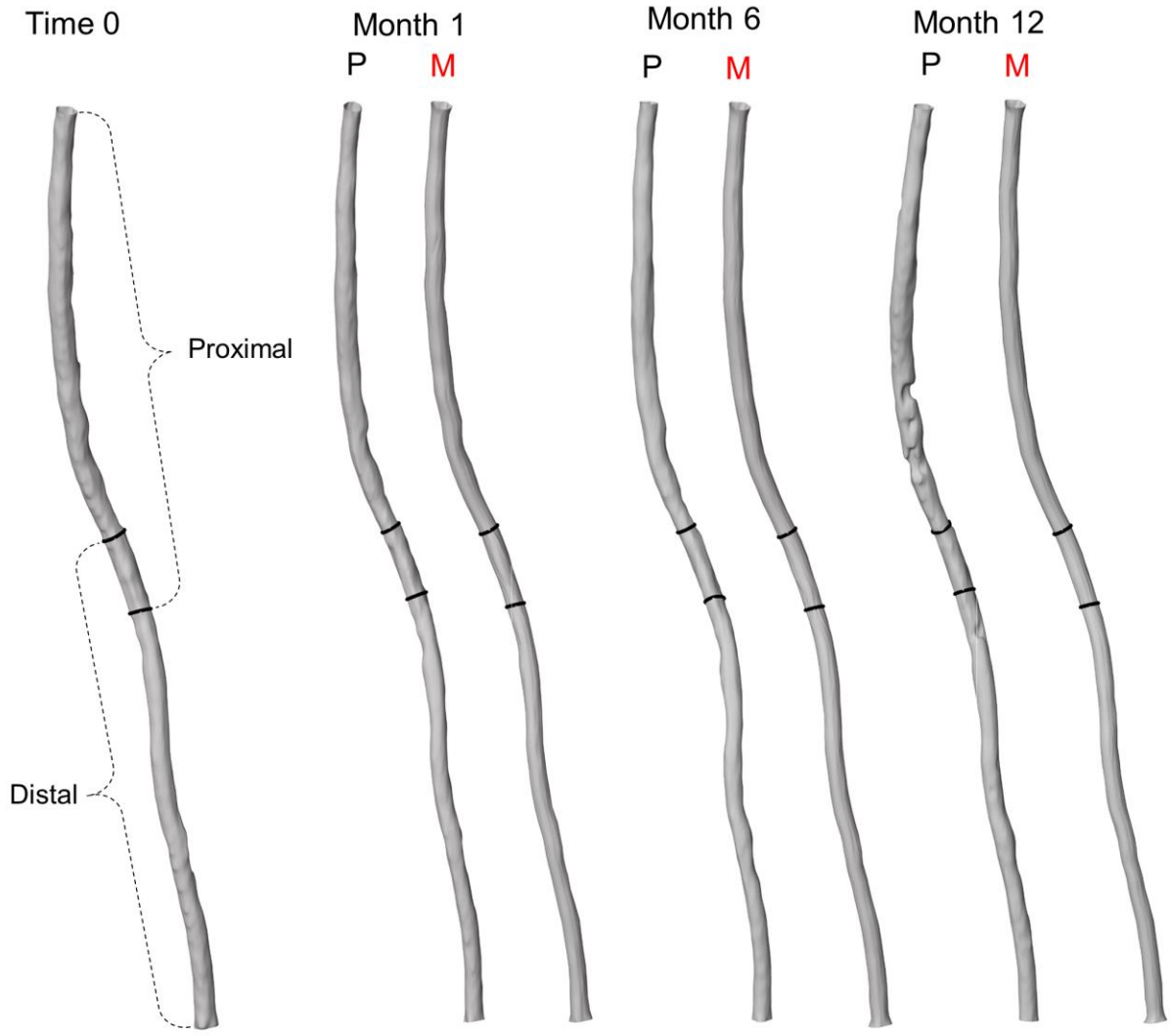
Time 0
Month 1
Month 6
Month 12
P
M
P
M
P
M
Proximal
Distal

Figure 10. Evaluation of the calibrated framework applied to the left distal stented superficial femoral artery lesion (lesion L-B). A) Boxplots of the lumen area of the stented portion immediately after the intervention (Time 0), at month 1 of the patient case (Month1-P) and of the calibrated model case (Month1-M), at month 6 of the patient case (Month6-P) and of the calibrated model case (Month6-M), and at month 12 of the patient case (Month12-P) and of the calibrated model case (Month12-M). Mann-Whitney U-test was used for pairwise comparisons. *p-value < 0.05. B) Comparison between the lumen geometries of the stented portion of the patient (reconstructed from computer tomography at the four available follow-ups), denoted as P, and of the model (generated from the ABM outputs at 1 month, 6 months and 12 months), denoted as M. Only the vessel region delimited by the proximal and distal stents is shown.

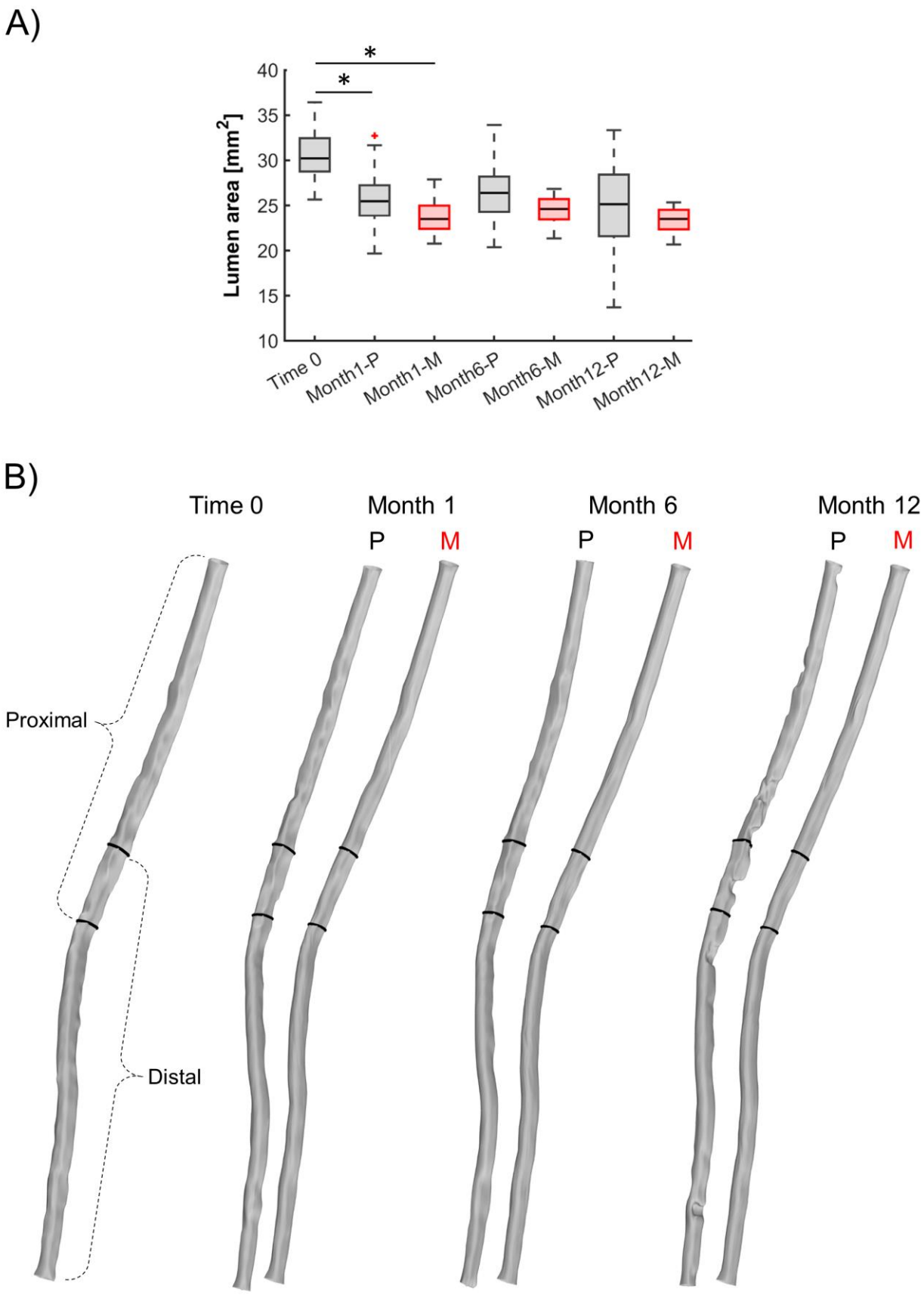
A)
Lumen area [mm^2]
40
35
30
25
20
15
10
*
*
Time 0
Month1-P
Month1-M
Month6-P
Month6-M
Month12-P
Month12-M
B)
Time 0
Month 1
Month 6
Month 12
P
M
P
M
P
M
Proximal
Distal

Figure 11. Evaluation of the calibrated framework applied to the right stented superficial femoral artery lesion (lesion R). A) Boxplots of the lumen area of the stented portion immediately after the intervention (Time 0), at month 1 of the patient case (Month1-P) and of the calibrated model case (Month1-M), at month 6 of the patient case (Month6-P) and of the calibrated model case (Month6-M), and at month 12 of the patient case (Month12-P) and of the calibrated model case (Month12-M). Mann-Whitney U-test was used for pairwise comparisons. *p-value < 0.05. B) Comparison between the lumen geometries of the stented portion of the patient (reconstructed from computer tomography at the four available follow-ups), denoted as P, and of the model (generated from the ABM outputs at 1 month, 6 months and 12 months), denoted as M. Only the vessel region delimited by the proximal and distal stents is shown.

Tables

Table 1. Agent-based model inputs and cellular activities.

WSSinput definition	$D(WSS)^i = -\frac{1}{1+e^{L_1(WSS^i - L_2)}} + 1$ $WSSinput = \begin{cases} D(WSS)^i & lumen \\ \sum_i D(WSS)^i \times Amp \times (1+\cos(\pi \frac{x}{dist})) & intima \end{cases}$
GEinput definition	$w_5 = -\frac{1}{1+e^{p_{ge} * \Delta_5}} + 1; \quad w_8 = \frac{1}{1+e^{p_{ge} * \Delta_8}}; \quad w_{24} = \frac{1}{1+e^{p_{ge} * \Delta_{24}}}$ $GEinput(t) = (w_5 \times w_8 \times w_{24}) \times Inflammation(t - delay)$
Cellular activity probabilistic rules	$intima: \begin{cases} p^h_{division} = \alpha_1 + \alpha_2 WSSinput^h + \alpha_3 GEinput^h \\ p^h_{apoptosis} = \alpha_1 \\ p^h_{ECMproduction} = \alpha_4 + \alpha_5 WSSinput^h + \alpha_6 GEinput^h \\ p^h_{ECMdegradation} = \alpha_4 / \beta_{int} \end{cases}$ $media/adv: \begin{cases} p^h_{division} = p^h_{apoptosis} = \alpha_1 \\ p^h_{ECMproduction} = \beta_{med/adv} \cdot p^h_{ECMdegradation} = \alpha_4 \end{cases}$

D(WSS): level of endothelial dysfunction; *WSS*: wall shear stress; L_1: slope of the logistic curve; L_2: WSS value at which D(WSS)=0.5; *WSSinput*: WSS-based input; *Amp*: scaling factor; *x*: distance of the intima site *i* from the lumen wall, $x < dist$; *dist* =15 constant; w_5: gene expression-based weight of cluster 5; w_8: gene expression-based weight of cluster 8; w_{24}: gene expression-based weight of cluster 24; p_{ge}: slope of the sigmoid function; Δ_5: difference between the patient-specific curve and average success curve for cluster 5; Δ_8: difference between the patient-specific curve and average success curve for cluster 8; Δ_{24}: difference between the patient-specific curve and average success curve for cluster 24; *GEinput*: gene expression-based input; *inflammation*: inflammatory curve; *delay* = 3 days; $p^h_{division}$: probability of cell mitosis; $p^h_{apoptosis}$: probability of cell apoptosis; $p^h_{ECMproduction}$: probability of extracellular matrix (ECM) production; $p^h_{ECMdegradation}$: probability of ECM degradation; α_1, α_2, α_3, α_4, α_5, α_6: parameters driving agent probabilities; β_{int} = 1.55, β_{med} = 1.55 and β_{adv} = 2.5.

Table 2. Agent-based model parameters.

Parameter	α_1	α_2	α_3	α_4	α_5	α_6	L_1	L_2	Amp	p_{ge}
Value – [range]	0.05	[0; 0.1]	[0; 1.7]	0.008	[0; 0.1]	[0; 1.77]	-15.25	0.5	[0.013; 0.13]	[-6; -2.5]

Table 3. Details on the patient lumen area and on the lumen area and normalized intimal extracellular matrix / smooth muscle cell ratio (ECM/SMC_{ratio_int}) obtained with the agent-based model (ABM) parameter combination #38.

	1-month Lumen area	**6-month Lumen area**	**1-month SCM/SMCratio_int**	**6-month SCM/SMCratio_int**
Patient	23.61 [22.68 25.79]	25.18 [20.32 25.98]	NA	NA
#38	23.70 [22.72 24.50]	23.04 [22.81 23.49]	1.49 [1.42 1.52]	0.98 [0.94 0.99]

Table 4. Calibrated agent-based model parameters.

α_2	α_3	α_5	α_6	**Amp**	p_{ge}
0.0325	1.1758	0.0175	0.8997	0.1114	-4.9208